Efficient dual-pathway H_2O_2 production promoted by covalent triazine frameworks with integrated dual active sites

Shasha Liu [a], Chao Zhu [a], Junjie Xu [a], Lun Lu [b], Qile Fang [c], Chao Xu [a], Yong Zheng [d], Shuang Song [a], Yi Shen [a,*]

[a] *Key Laboratory of Microbial Technology for Industrial Pollution Control of Zhejiang Province, College of Environment, Zhejiang University of Technology, Hangzhou 310032, PR China*
[b] *State Environmental Protection Key Laboratory of Environmental Pollution Health Risk Assessment, South China Institute of Environmental Sciences, Ministry of Ecology and Environment, Guangzhou 510655, PR China*
[c] *Advanced Institute of Natural Sciences, Beijing Normal University at Zhuhai, Zhuhai 519087, PR China*
[d] *College of Materials and Chemical Engineering, China Three Gorges University, Yichang 443002, PR China*

ARTICLE INFO

ABSTRACT

The dual-pathway direct 2e- redox reaction is considered an efficient route for the photocatalytic generation of hydrogen peroxide (H_2O_2). However, the targeted design of catalysts to achieve dual-pathway reaction remains a scientific bottleneck. Herein, dual active site covalent triazine frameworks incorporating single-atom Ni and pyridine N was constructed (d-CTF-Ni), with the dual-pathway synergistically promoting H_2O_2 generation through oxygen reduction and water oxidation reaction. Furthermore, the pivotal role of electron transfer in enhancing catalytic activity was elucidated. Due to the presence of electron-capture centers Ni atoms and hole acceptors pyridine N, d-CTF-Ni exhibited a pronounced augmentation in the rate of H_2O_2 generation in pure water (869.1 $\mu mol \cdot g^{-1} \cdot h^{-1}$), accompanied by excellent stability in multi-cycle. Experimental results and theoretical calculations indicate that the electron deficiency of N atom in pyridine promotes hole accumulation, while the single-atom Ni provides a directional pathway (Ni→O_2) for electron transfer, thereby collectively accelerating the reaction. This study provides new insights into the electron behavior in H_2O_2 production at material interfaces and offers a new perspective on the dual-pathway 2e- redox mechanism in understanding photocatalytic H_2O_2 generation.

1. Introduction

Solar-driven photocatalytic processes offer a sustainable and environmentally benign approach for hydrogen peroxide (H_2O_2) production, with considerable promise in environmental applications [1,2]. Consequently, numerous photocatalysts have been synthesized using diverse modification strategies to date [3]. However, the sluggish kinetics of H_2O oxidation reaction and the limited selectivity of O_2 reduction reaction pose significant constraints on the efficiency of H_2O_2 production through a single reaction pathway [4,5]. Actually, multiple pathways may coexist in process of H_2O_2 production [6], underscoring the importance of enhancing the selectivity towards the desired target pathway.

Indeed, the oxygen reduction reaction (ORR) can be categorized into two distinct types based on the number of electron transfers and reaction intermediates involved that the direct one-step two-electron oxygen reduction reaction (direct 2e--ORR, $O_2 + 2 H^+ + 2e^- \rightarrow H_2O_2$), and the sequential two-step indirect two-electron oxygen reduction reaction (indirect 2e--ORR, $O_2 + e^- \rightarrow \cdot O_2^- + e^- + 2 H^+ \rightarrow H_2O_2$) [7]. The direct 2e--ORR, owing to its thermodynamic advantage, displays a faster reaction rate [8]. Nevertheless, intermediates$\cdot O_2^-$ generated in the indirect 2e--ORR would compete for electrons with the direct 2e--ORR pathway [9,10], and the strong oxidizing properties lead to partial photocatalyst damage, impeding the progress of photocatalytic reactions [11]. Hence, enhancing the selectivity towards the direct 2e--ORR is of paramount importance for the efficient production of H_2O_2. Moreover, it is worth noting that H_2O_2 can also be produced via the frequently disregarded water oxidation reaction. (WOR, $2 H_2O + 2 h^+ \rightarrow H_2O_2 + 2 H^+$) [12]. In the absence of sacrificial agents, the concurrent dual-pathway production of H_2O_2 can be achieved by synergistically coupling the WOR with

---

* Corresponding author.
E-mail address: shenyi@zjut.edu.cn (Y. Shen).

the ORR [13,14], in which the hydrogen proton (H^+) generated through WOR participates in ORR, and in turn ORR provides more hole (h^+) for WOR, avoiding the extra expenses and complexities came from sacrificial agents. In general, the dual-pathway coupling of 2e$^-$-ORR and 2e$^-$-WOR offers the potential to achieve theoretically 100% atomic utilization efficiency [15].

Despite extensive exploration in the field of photocatalytic production of H_2O_2, only a few heterogeneous catalysts have successfully realized dual-pathway reactions [16]. For instance, in heterojunction CN-CRCDs, carbon nitride (CN) performs ORR meanwhile hexachlorocyclohexane-derived carbon dots (CRCDs) execute WOR, with the combination of electrons and holes at the heterogeneous interface preventing the depletion of original electrons in CN and original holes in CRCDs, thus leading to a significant enhancement in catalytic efficiency [17]. The catalyst CN$_{1.8}$/ICT/CDs, with organic small molecules (ICT) as the ORR active site and carbon dots (CDs) as the WOR active site, exhibits excellent hydrophilicity and resistance to H_2O_2 poisoning, enabling efficient and stable H_2O_2 production through dual-pathway processes [18]. However, the differences between components and the ambiguity of active centers present formidable obstacles in precisely controlling the specificity of active sites and the directionality of charge transfer. Therefore, the pressing requirement involves the construction of spatially isolated active sites that facilitate targeted reactions without reciprocal interference, thereby promoting more directed electron transfer and ultimately elevating the reactivity performance.

With well-defined active centers and high π-electrons density, covalent organic frameworks (COFs) [19], have emerged as promising materials for achieving targeted functionalities through precise precursor modulation [20]. However, the homogeneous distribution of π-electrons and low intramolecular dipole moments in regular COFs impose constraints on the potential for efficient redox properties [21]. Recent research has been dedicated to regulating the π-electron structure in COFs to construct active sites with oxidative properties. The covalent triazine frameworks (CTFs), as a kind of COFs with the introduction of triazine to build π electron-deficient structures, not only enhances charge generation and separation but also enriches the photocatalytic active sites, thereby facilitating efficient and selective oxidation of sulfides [22]. Through the incorporation of pyridine in the CTF, the directionality of electron transfer is augmented, whereby the π-deficient pyridine units function as electron donors, thereby facilitating oxidative degradation [23]. For example, the pyridine unit in M-CTF promotes electron donation to effectively enhance the directionality of electron transfer, further facilitating photocatalytic oxidative degradation of organic pollutants [24]. Moreover, anchoring metal single-atom can profoundly modulate the electronic structures and the separation of photogenerated electron-hole in catalysts, thus promoting reducibility [25]. For instance, the coordination of monoatomic Fe with g-C$_3$N$_4$ through Fe-N$_4$ establishes a novel electron transfer pathway, resulting in a substantial enhancement in carrier separation and promoting the generation of superoxide radicals through reduction reactions [26]. Nonetheless, the π-electronic structure modulation and the utilization of anchored single-atom metals in CTFs for dual-pathway photocatalytic H_2O_2 production by coupling of 2e$^-$-ORR and 2e$^-$-WOR has been relatively underexplored, and the intrinsic mechanism remains obscure.

Although the promising performance of catalytic systems capable of dual-pathway H_2O_2 production, such as ZIF-8/g-C$_3$N$_4$ (2641 μmol·g^{-1}·h^{-1}) [27], HTMT-CD (4240 μmol·g^{-1}·h^{-1}) [28], and CPN (1968 μmol·g^{-1}·h^{-1}) [29], the underlying mechanisms governing dual active sites and dual-pathway remain inadequately explored. Herein, aiming at the photocatalytic production of H_2O_2 through the dual-pathway of 2e$^-$-ORR and 2e$^-$-WOR, the d-CTF-Ni was synthesized by incorporating Ni single atoms served as electron-capture centers and pyridine N served as hole acceptors. Due to the presence of dual active centers, d-CTF-Ni exhibited a high H_2O_2 production rate of 869.1 μmol·g^{-1}·h^{-1} in pure water, surpassing most reported visible-light-driven catalysts. Theoretical calculations unveiled that the electron deficiency of N atoms in pyridine promotes hole accumulation, while the single-atom Ni provides a directional pathway for electron transfer, thus cooperatively enhancing the photocatalytic H_2O_2 performance. This work provides new insights into the rational design of functional materials and presents an innovative idea for comprehending the intricacies involved in the dual-pathway mechanisms of photocatalytic H_2O_2 production.

2. Experimental section

2.1. Synthesis of p-CTF and d-CTF

The pristine CTF (p-CTF) was synthesized by dissolving 5.5 mmol of 1,4-dicyanobenzene in 3 mL of trifluoromethanesulfonic acid (CF$_3$SO$_3$H) at 0 °C. After stirring for 1.5 h and heating at 100 °C for 20 min, distinctive yellow crystals formed. The sample underwent alternating washing cycles with distilled water and ethanol to eliminate residual monomers and acidic remnants. Centrifugation at 10,000 rpm for 5 min removed unreacted components and acidic residues. The extensively rinsed p-CTF was subjected to drying at 60 °C for 24 h and subsequently pulverized into a fine powder. To produce the triazine-deficient CTF (d-CTF), 5.5 mol of 1,4-dicyanobenzene was replaced with a mixture of 5.2 mmol of 1,4-dicyanobenzene and 0.3 mmol of 4-cyanopyridine. The subsequent procedures remained unchanged, resulting in the production of triazine-deficient d-CTF.

2.2. Synthesis of p-CTF-Ni and d-CTF-Ni

The preparation steps for p-CTF-Ni and d-CTF-Ni are identical, and d-CTF-Ni was used as an example. Initially, 100 mg of d-CTF was combined with 6 mL of ethylene glycol at room temperature for 30 min. Afterward, the resulting mixture was carefully transferred into a 20 mL Teflon-lined stainless-steel autoclave and hermetically sealed. The autoclave was then subjected to a temperature of 150 °C for a duration of 4 h, followed by gradual cooling to reach ambient room temperature. The resulting white product was washed with distilled water and ethanol, followed by collection through centrifugation at 10,000 rpm for 5 min. The sample was subsequently subjected to vacuum drying in an oven at 60 °C for 24 h to yield the hydroxyl-functionalized covalent triazine framework (hy-d-CTF).

The Ni-based CTF was prepared using the following procedure. Initially, 120 mg of hy-d-CTF was dispersed in 10 mL of water within a 20 mL glass bottle. With continuous stirring, 70 μL of Nickel nitrate hexahydrate (Ni(NO$_3$)$_2$·6 H$_2$O, 10 mg·mL^{-1}) was added. The diameter of the glass bottle was approximately 2 cm, smaller than the spot diameter of the mercury lamp parallel light source system (~5 cm). Following UV irradiation for 30 min, the samples underwent centrifugation, were washed twice with distilled water, and subsequently subjected to vacuum drying at 60 °C for 24 h, resulting in the formation of UV-d-CTF. Finally, the UV-d-CTF was roasted in the air at 180 °C for 2 h, with a ramp rate of 3 °C·min^{-1}, resulting in the formation of d-CTF-Ni.

2.3. Photocatalytic experiments

The photocatalytic H_2O_2 production experiment was conducted in a glass beaker. A quantity of 20 mg of catalyst was dispersed in 50 mL of distilled water and stirred in the dark while being bubbled with 50 mL·min^{-1} of O_2 for 30 min to establish an adsorption-desorption equilibrium. Subsequently, continuous stirring was maintained at 25 ℃. The illuminated system underwent exposure to a 300 W xenon lamp (100 mW·cm^{-2}) for 3 h with a 420 nm filter. Throughout the experiment, the suspension was continuously pumped at a rate of 40 mL·min^{-1} of O_2. To remove the photocatalyst, 5 mL of solvent was sampled every 30 min and filtered using a 0.45 μm filter. The concentration of H_2O_2 was
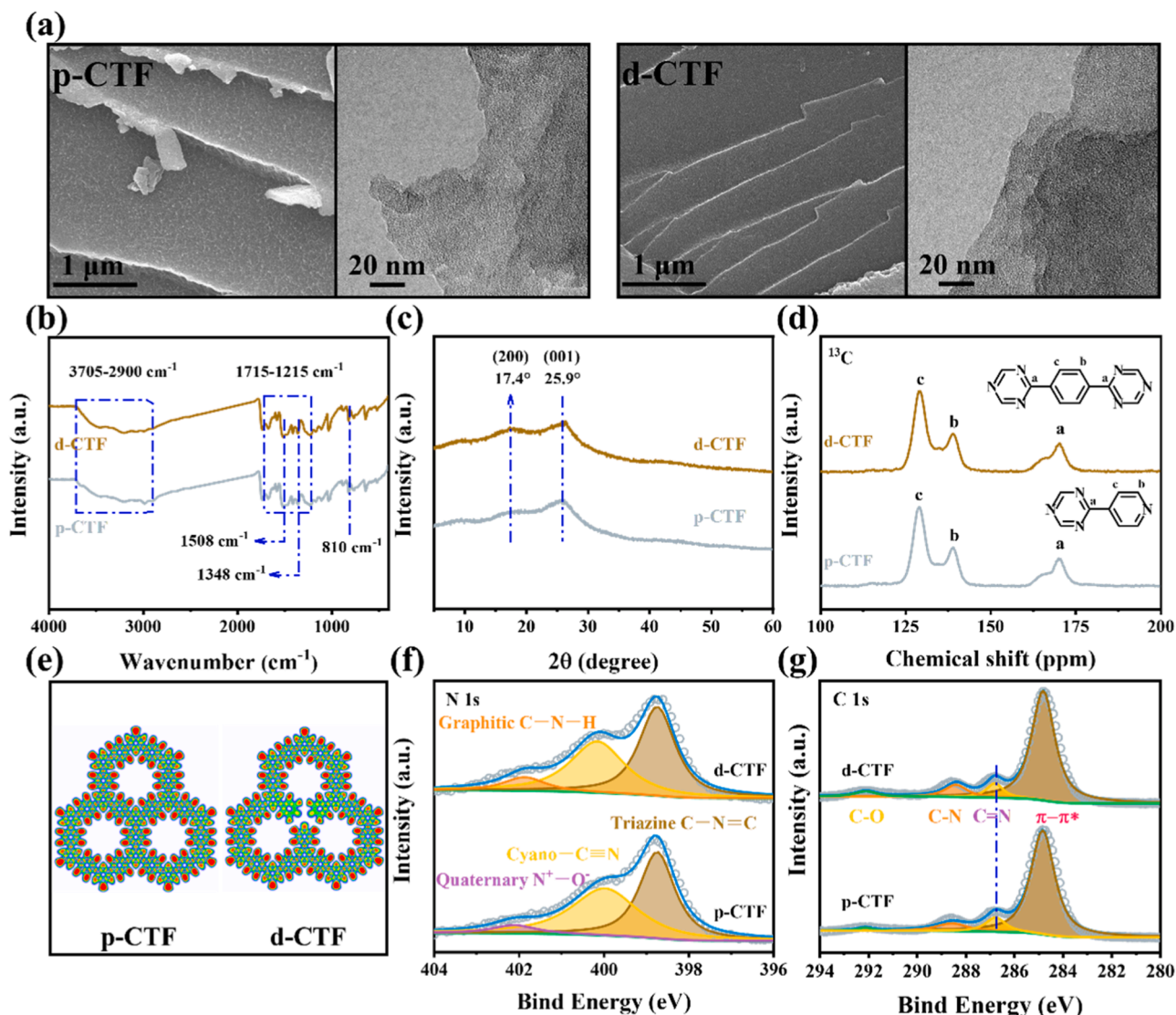
Fig. 1. (a) FE-SEM and HR-TEM images of p-CTF and d-CTF. The spectra of (b) FTIR, (c) XRD, and (d) ^{13}C MAS solid state NMR. (e) ELF plot of p-CTF and d-CTF. (f) XPS N 1 s spectra of p-CTF and d-CTF. (g) XPS C 1 s spectra of p-CTF and d-CTF.

determined through potassium titanium oxalate and iodine assay.

Quenching experiments were conducted using various scavengers, namely silver nitrate ($AgNO_3$) as an electron scavenger (e^-), ethylenediaminetetraacetic disodium salt (EDTA-2Na) as a photogenerated hole scavenger (h^+), tert-butanol (TBA) as a hydroxyl radical scavenger ($\cdot OH$), and benzoquinone (p-BQ) as a superoxide radical scavenger (O_2^-). The quenching experiments were performed under the same conditions as the photocatalytic experiments, with the addition of 1 mmol of the respective scavenger.

2.4. Characterization

The morphology and physical properties of the catalysts were characterized using Field Emission Scanning Electron Microscopy (FESEM), High-Resolution Transmission Electron Microscopy (HRTEM), X-ray diffraction (XRD), and High-Angle Annular Dark-Field Scanning Transmission Electron Microscopy (HAADF-STEM). The chemical structure was probed using Fourier Transform Infrared Spectroscopy (FT-IR), X-ray Photoelectron Spectroscopy (XPS), X-ray Absorption Near-Edge Structure (XANES), and Extended X-ray Absorption Fine Structure (EXAFS) measurements. The photoelectrochemical and electrochemical properties were evaluated by methods including photoluminescence

(PL) spectra, electrochemical impedance spectroscopy (EIS), periodic on/off photocurrent responses, Mott−Schottky plots, and UV−visible diffuse-reflectance spectra (UV−vis DRS). The radical species in the photocatalytic process were detected by electron spin resonance (ESR) spectroscopy. Additional details were encompassed in the supplementary information (SI).

2.5. DFT computational

The Vienna Ab Initio Package (VASP) was performed for all density functional theory (DFT) calculations using the PBE formulation in the generalized gradient approximation (GGA). The projection enhanced wave (PAW) potentials were chosen to describe the ionic cores and the valence electrons were taken into account using a plane wave basis set with a kinetic energy cutoff of 400 eV. The use of Gaussian smearing and a width of 0.05 eV allowed for partial occupancies of the Kohn-Sham orbitals. The electron energy was considered self-consistent when the change in energy was less than 10^{-5} eV. The optimization of geometry was considered convergent when the change in force was smaller than $0.02 \text{ eV} \cdot \text{Å}^{-1}$. Grimme's DFT-D3 method was used to describe the dispersive interactions. Additional details were provided in the supporting information (SI).
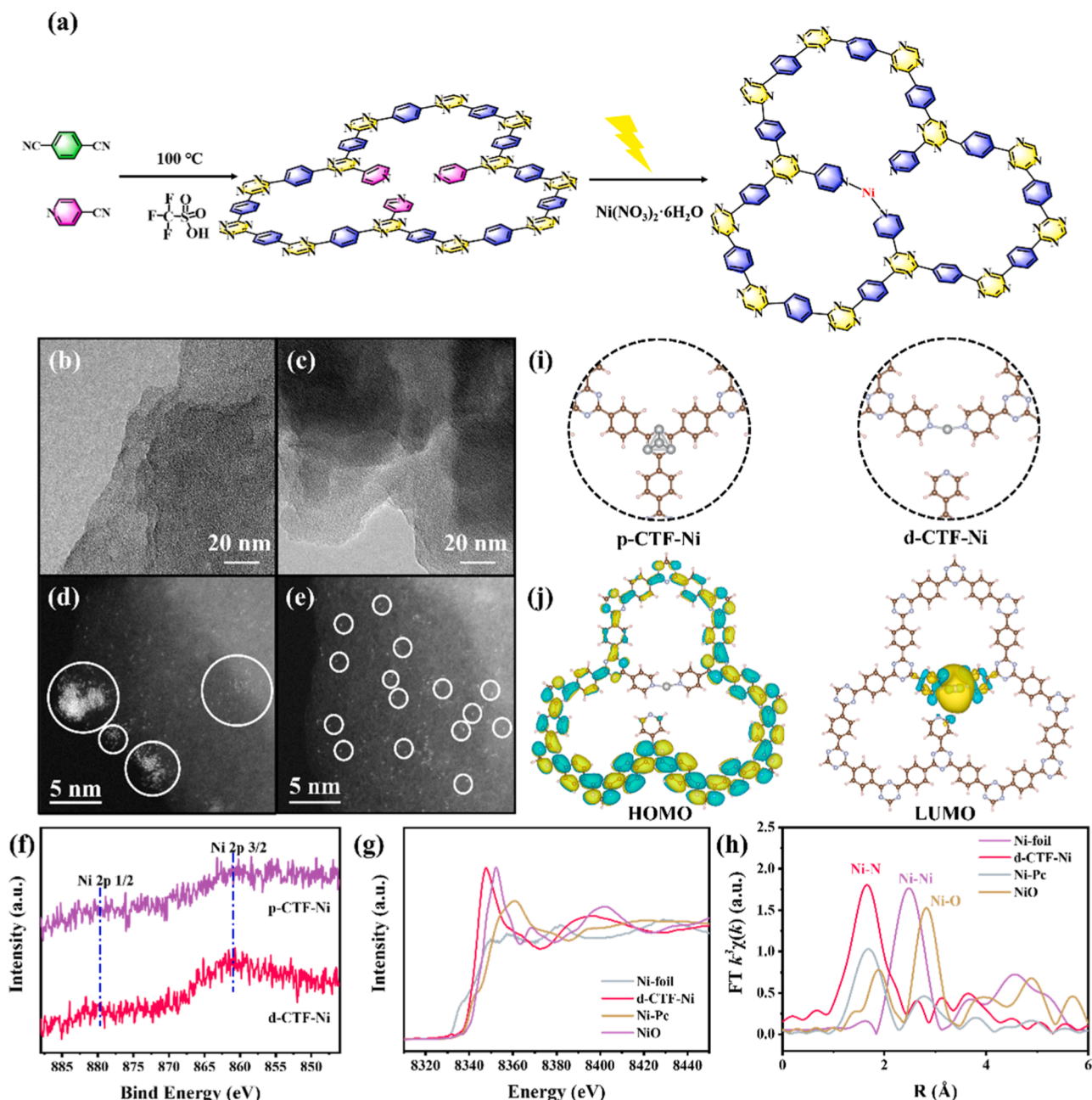
Fig. 2. (a) The synthesis strategy and structure of d-CTF-Ni. HR-TEM image of (b) p-CTF-Ni and (c) d-CTF-Ni. AC HAADF-STEM image of (d) p-CTF-Ni and (e) d-CTF-Ni. (f) XPS Ni 2p spectra of p-CTF-Ni and d-CTF-Ni. (g) Ni K-edge XANES spectra of d-CTF-Ni compared to standard NiO, NiPc, and Ni foil. (h) The plotted Fourier transformation of the extended X-ray absorption fine structure (FT-EXAFS) spectra of d-CTF-Ni, Ni-foil, NiPc and NiO. (i) Theoretical models for p-CTF-Ni and d-CTF-Ni. (j) HOMO and LUMO of d-CTF-Ni.

3. Results and discussion

3.1. Structural characterization of p-CTF and d-CTF

The different CTFs, namely p-CTF and d-CTF, were prepared by modifying the precursor species using a strong acid polymerization method. The FE-SEM and HR-TEM images (Fig. 1a) reveal that both p-CTF and d-CTF possess unique sheet-like structures [30], and Table S1 indicates that the specific surface areas of the two materials are comparable. These structural characteristics enable p-CTF and d-CTF as promising platforms for facilitating photocatalytic reactions. In particular, d-CTF (10.471 nm) has a larger specific pore size than p-CTF (0.054 nm) (Table S1), which is because the defects in the d-CTF cause the unit junctions breaking off to form larger units and thus improving

the pore size [31]. In contrast, the difference in the molecular structure of the catalysts was subsequently verified through Fourier transform infrared (FTIR) and X-ray diffraction (XRD) spectroscopy. The characteristic peak at 810 cm^{-1} and the range of 1215–1715 cm^{-1} corresponded to the stretching modes of benzene and aromatic C-N heterocycles, respectively (Fig. 1b), thereby confirming the existence of benzene and triazine rings [24,32]. Meanwhile, two obvious peaks of d-CTF at 1508 and 1348 cm^{-1} are weaker than those of p-CTF, which is associated with C-N stretching vibrations and triazine ring vibrational modes, respectively, suggesting the presence of defects in d-CTF [33]. The XRD spectra (Fig. 1c) reveal the semi-crystalline characteristics of both p-CTF and d-CTF, as evidenced by the presence of two prominent peaks at 17.4° and 25.9°, corresponding to the (200) plane associated with planar spacing and the (001) plane related to interlayer spacing,
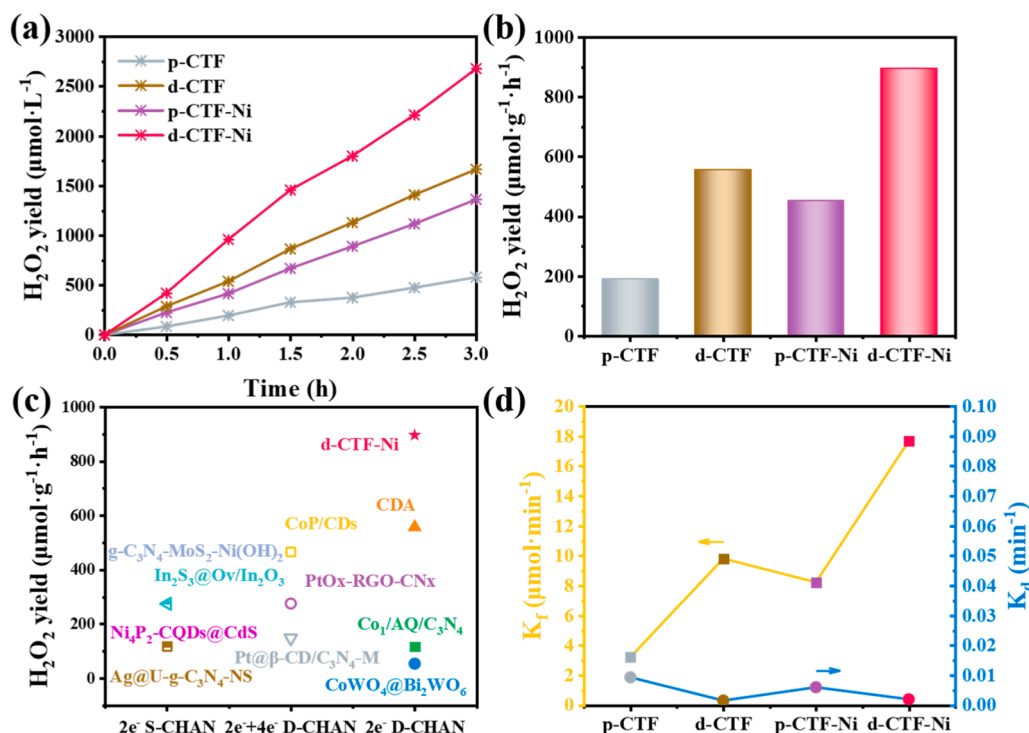
Fig. 3. (a) The time profiles of H_2O_2 production by various catalysts were tested under visible light irradiation. (b) The yield of H_2O_2 for each catalyst was tested over 3 h. (c) The H_2O_2 production was compared with the results of recent research exploring different mechanisms. These mechanisms were grouped as follows: $2e^-$ S-CHAN, representing the $2e^-$ single-pathway transfer involving oxidation or reduction; $2e^- + 4e^-$ D-CHAN, representing the dual-pathway transfer involving both $2e^-$ and $4e^-$ redox; and $2e^-$ D-CHAN, representing the dual-pathway transfer involving only $2e^-$ redox reactions. (d) The rate constants for H_2O_2 formation (K_f) and decomposition (K_d) were determined and compared across catalysts.

respectively [34]. The slightly intensified inter-surface spacing signal and the marginally shifted interlayer spacing signal observed in the d-CTF compared to the p-CTF suggest that the presence of defects may induce alterations in the ordered structure within the framework [35]. As shown in Fig. 1d, the composition of the ^{13}C MAS solid state nuclear magnetic resonance (NMR) spectra remain unchanged, indicating that the lack of component in d-CTF is the intact triazine ring, with the noteworthy observation that the reduce of the intact triazine ring does not exert any influence on the peak shape. The ^1H NMR spectra reveals peaks around 7 ppm (Fig. S1), corresponding to all the CH groups on the benzene rings, triazine rings, and pyridine rings. The intensity and area of these peaks in d-CTF are lower than those in p-CTF, indicating the presence of defects in d-CTF. However, the defects in d-CTF lead to lattice distortion, resulting in changes in the intensity of the Raman spectra (Fig. S2). Additionally, the electron localization function (ELF) plot (Fig. 1e) also reveals that these defects induce charge redistribution, with a decrease in π-electron density near the pyridine N sites adjacent to the defect edges [36]. Moreover, X-ray photoelectron spectroscopy (XPS) analysis provides a profound understanding of the changes in the elemental composition of the catalyst. As shown in Fig. 1f, the XPS N 1 s spectra can be divided into four distinct peaks. Compared to p-CTF (49.2%), the lower content of triazine nitrogen (C-N = C, 398.7 eV) in d-CTF (40.8%) indicates the lack of the triazine structure in the d-CTF catalyst (Table S2) [37]. Based on the above analysis, the reduction in triazine rings within d-CTF is achieved by altering the precursor. A triazine ring is synthesized via cyanide polymerization, and the introduction of pyridine leads to the substitution of the triazine ring initially formed by cyanide, resulting in the existence of three distinct pyridine rings. Additionally, in the XPS C 1 s spectra (Fig. 1g), the increased binding energy of C≡N in d-CTF compared to p-CTF suggests that the presence of pyridine N enhances the electron density of carbon and nitrogen atoms (Table S3) [38]. Due to the lower electronegativity and significant loss of π electrons in pyridine N, it exhibits the characteristics

of a hole acceptor within the molecular framework. Therefore, with the presence of exposed pyridine N at defect edges, d-CTF can utilize the π electron deficiency of pyridine N, making it a potential oxidation center.

3.2. Structural characterization of p-CTF-Ni and d-CTF-Ni

Ni-based photocatalysts, namely p-CTF-Ni and d-CTF-Ni, were synthesized using p-CTF and d-CTF as the precursor materials, respectively (Fig. 2a). The HR-TEM images revealed that both p-CTF-Ni and d-CTF-Ni maintained the sheet-like morphology resembling the metal-free CTF, and no metal particles were observed, indicating the absence of Ni nanoparticles in p-CTF-Ni and d-CTF-Ni (Fig. 2b-c). Moreover, Ni-based catalysts exhibit differences in the XRD and FTIR spectra compared to p-CTF and d-CTF (Figs. S3–4). In the FTIR spectra, both p-CTF-Ni and d-CTF-Ni show a decrease in vibrational intensity in the range of $3705–2900\ cm^{-1}$ corresponding to the C-H vibrations in the pyridine ring, indicating the interaction of the -CN in pyridine with Ni atoms. In the XRD spectra, p-CTF-Ni and d-CTF-Ni display a shift in the diffraction peak signal at the (200) plane, and new diffraction peaks attributed to the (100) plane appear at lower angles, suggesting a change in the interplanar spacing of the CTF framework and the emergence of lattice fluctuations [39]. The above results collectively confirm the presence of Ni atoms within the frameworks of both p-CTF-Ni and d-CTF-Ni. Additionally, the ^{13}C NMR spectra of p-CTF-Ni and d-CTF-Ni also confirm that the anchoring of Ni atoms did not induce significant structural changes in the original frameworks of d-CTF and p-CTF (Fig. S5). To further confirm the dispersed state of Ni atoms, the aberration-corrected high-angle annular dark-field scanning transmission electron microscopy (AC HAADF-STEM) was conducted. The AC HAADF-STEM images of p-CTF-Ni (Fig. 2d) showed bright spots clustered together, while d-CTF-Ni (Fig. 2e) exhibited individual bright spots. It can be inferred that the presence of defects resulted in the significant dispersion of Ni atoms on the CTF framework, effectively preventing the microscale
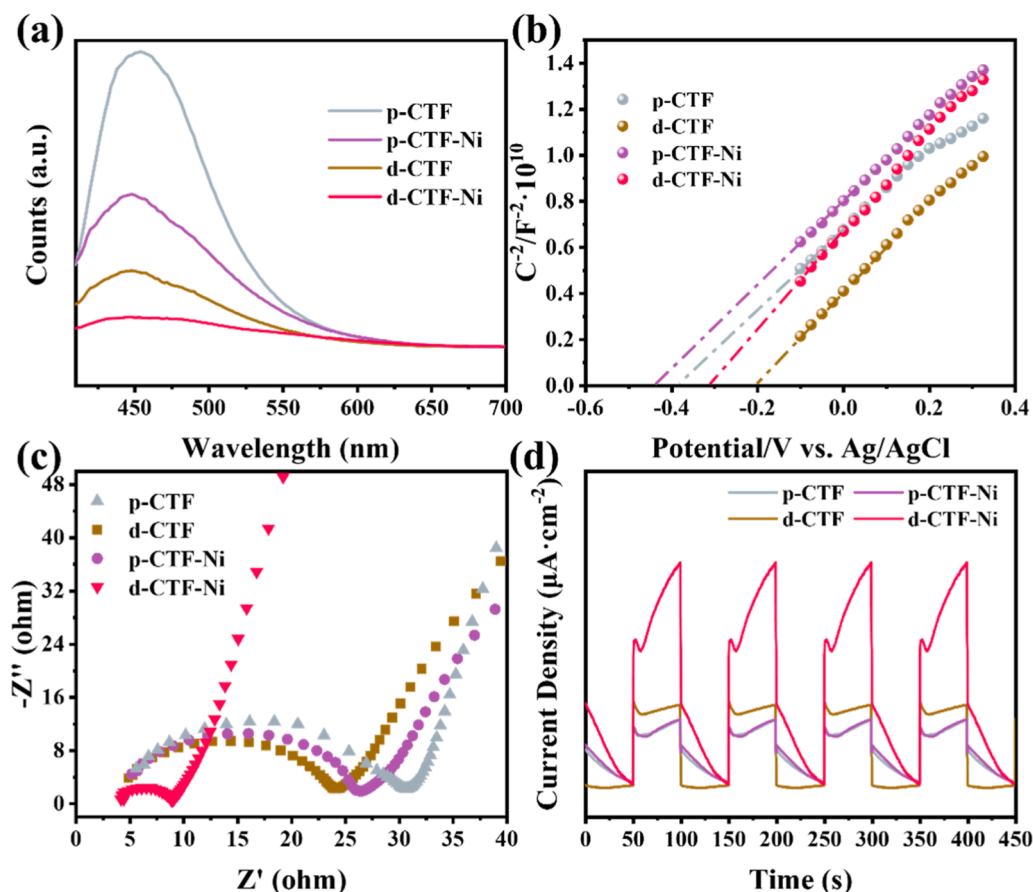
Fig. 4. (a) PL spectra of catalysts. (b) Mott-Schottky plot for catalysts. (c) EIS Nyquist plots and (d) transient photocurrent response curves of catalysts.

aggregation of individual Ni metal atoms. However, there was a difference in the metal content between p-CTF-Ni and d-CTF-Ni, with Ni contents of 0.51% and 0.23%, respectively, as determined by inductively coupled plasma optical emission spectroscopy (ICP-OES). Additionally, XPS analysis of Ni 2p revealed that Ni was primarily attributed to dispersed Ni^{2+} and Ni^{3+} species (Fig. 2f) [40]. To investigate the bonding states of Ni in p-CTF-Ni and d-CTF-Ni, the XPS spectra of C 1 s and N 1 s were analyzed. Fig. S6 shows that the introduction of Ni led to increased binding energy of C≡N, indicating electron loss from C or N through chemical bonding, implying the interaction between Ni atom and C or N atom. Besides, Fig. S7 displayed a reduction in the convolution area and an increase in the binding energy of N 1 s due to the presence of Ni, suggesting a decrease in pyridine N and strong interactions between Ni and N atoms [41]. The electronic structure and coordination environment of d-CTF-Ni were determined through Ni K-edge XANES and EXAFS tests. The pre-edge curve of d-CTF-Ni closely resembles that of NiPc and NiO (Fig. 2g), indicating a similar valence state for Ni in them. The Fourier-transformed k^3-weighted spectra of d-CTF-Ni at 1.67 Å reveals a prominent peak attributed to the coordination shell of Ni-N (Fig. 2h). This observation supports the presence of dispersed Ni atoms at Ni-N sites. Through the EXAFS fitting based on the Ni-N shell on d-CTF-Ni, an average coordination number of 2.2 has been determined (Table S4), indicating that Ni atoms in d-CTF-Ni coordinate with two N atoms at a bond length of 1.89 Å, consistent with the proposed DFT model (Fig. S8). Based on the analysis, it can be confirmed that Ni is bound to N at the defect site, forming a Ni-N bond that serves as the structural foundation for electron transfer. The stable structure of d-CTF-Ni was further determined using density functional theory (DFT), where a single Ni atom is coordinated with two N atoms, with a Ni-N bond length of 1.84 Å (Fig. 2i). Moreover, analysis of the frontier molecular orbitals of d-CTF-Ni reveals that the highest occupied molecular orbital (HOMO) is localized on the Ni atom and its adjacent pyridine ring, while the lowest unoccupied molecular orbital (LUMO) is located on the triazine and benzene rings (Fig. 2j). The distinct separation between HOMO and LUMO suggests the potential presence of separate redox centers in d-CTF-Ni [42]. It is speculated that the presence of independent electron-capture centers and hole acceptors in d-CTF-Ni may provide structural support for the promotion of H_2O_2 generation.

Through the above analysis, p-CTF-Ni and d-CTF-Ni, containing Ni atomic clusters and dispersed Ni atoms, respectively, were successfully synthesized based on the pristine CTF (p-CTF) and d-CTF with pyridine N structures. Among them, d-CTF-Ni contains both electron-capture centers and hole acceptors. Due to the deficient π electrons, the pyridine N are expected to be the active oxidation centers, while the Ni atoms are capable of capturing electrons and may become active reduction centers.

3.3. Photocatalytic production of H_2O_2 performance

A series of experiments were conducted under visible light illumination ($\lambda > 420$ nm) to investigate the influence of Ni atoms and pyridine N on the performance of the photocatalyst in producing H_2O_2. Negligible H_2O_2 production was observed in the absence of the catalyst or the dark, indicating the crucial role of the photocatalyst in H_2O_2 generation under visible light irradiation (Fig. S9). Fig. 3a illustrates the production of H_2O_2 over time under visible light. The H_2O_2 yields within 3 h are presented in Fig. 3b, showing the following order of d-CTF-Ni > d-CTF > p-CTF-Ni > p-CTF. It is noteworthy that p-CTF exhibits the lowest H_2O_2 production rate, while d-CTF and p-CTF-Ni which contain an active center, demonstrate significantly higher yields compared to p-CTF. Specifically, d-CTF-Ni with dual active sites, exhibits the highest H_2O_2 production in pure water, surpassing the performance of most

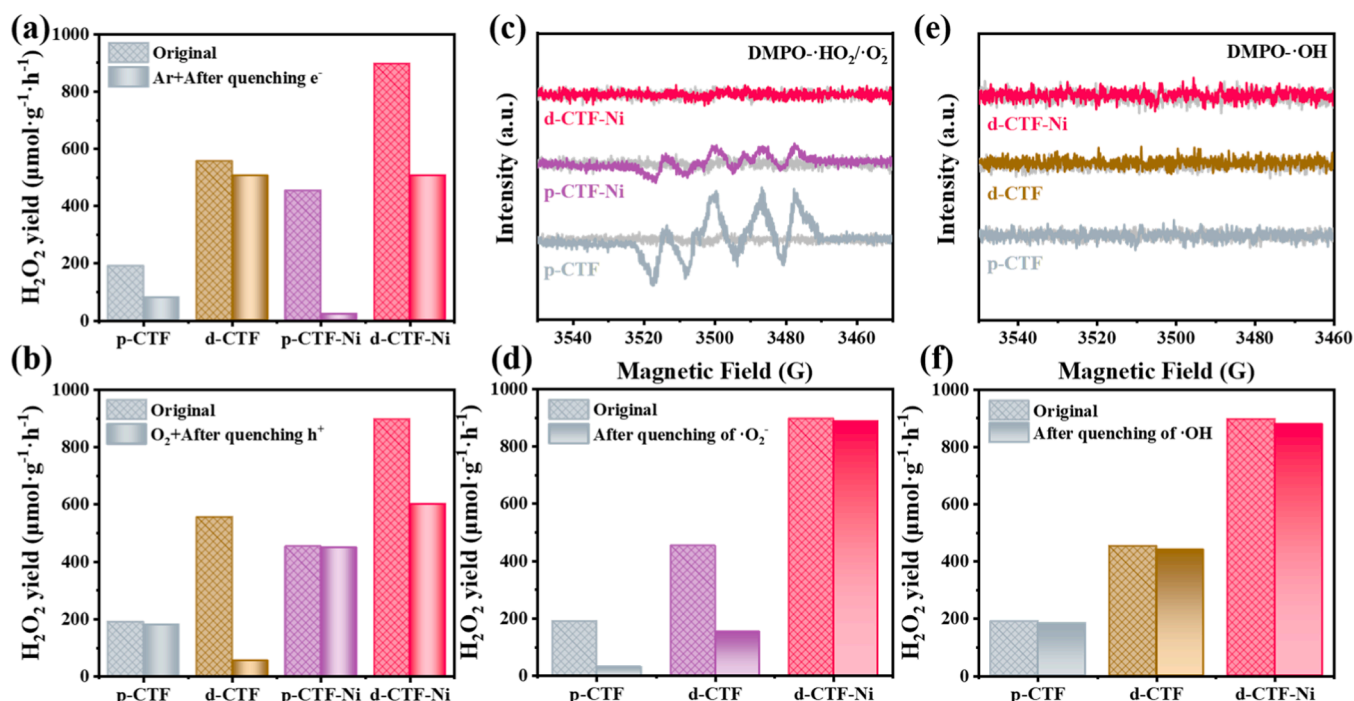**Fig. 5.** (a) Comparison of H_2O_2 yield before and after quenching h^+. (b) Comparison of H_2O_2 yield before and after quenching e^-. (c) EPR test for·O_2 during H_2O_2 production. (d) Comparison of H_2O_2 yield before and after quenching of·O_2. (e) EPR test for·OH during H_2O_2 production. (f) Comparison of H_2O_2 yield before and after quenching of·OH.

catalysts currently (Fig. 3c, Table S4). The appropriate VB position and effective electron-hole separation in d-CTF-Ni meet the requirements of the WOR for oxidation potential and H^+ quantity. And the H^+ generated in the WOR can participate in the ORR to produce more H_2O_2. Furthermore, the consumption of e^- in the ORR process partially impedes the recombination of charge carriers, thereby exposing more h^+ for involvement in the WOR. Therefore, the dual-pathway can generate more H_2O_2 by coupling the WOR and ORR, which is the reason behind the outstanding performance of d-CTF-Ni. This enhanced performance can be attributed to the presence of Ni atoms and pyridine N in d-CTF-Ni, which facilitate redox reactions during the H_2O_2 generation process. Additionally, the photocatalytic production of H_2O_2 is a dynamic process, where the generated H_2O_2 may simultaneously undergo decomposition through reactions with the electrons or holes generated by the photocatalyst. To gain a more comprehensive understanding of this dynamic photocatalytic process, rate constants for H_2O_2 generation (K_f, $\mu mol \cdot min^{-1}$) and decomposition (K_d, min^{-1}) were calculated, corresponding to zero-order and first-order kinetics, respectively. Based on the values of K_f and K_d obtained from the equation $[H_2O_2] = (K_f/K_d)\{1-exp(-K_d \cdot t)\}$ (Fig. 3d), d-CTF-Ni exhibits the highest K_f but the lowest K_d [43], indicating the most significant overall H_2O_2 production compared to other catalysts. Therefore, the production of H_2O_2 is not only enhanced by the presence of Ni atoms and pyridine N structures, but also hindered by its decomposition under light irradiation. Furthermore, the stability and high efficiency of d-CTF-Ni were confirmed through four cycles of repetitive experiments (Fig. S10), indicating its potential practical application in photocatalytic H_2O_2 production.

3.4. Photoelectrochemical analysis

The photochemical properties of these catalysts were investigated through photoelectric experiments. Photoluminescence (PL) spectroscopy was employed as an effective method to investigate the recombination of photogenerated electrons and holes [44]. It was observed that d-CTF-Ni exhibited the lowest steady-state PL intensity, indicating that the presence of Ni atoms and pyridine N facilitated charge carrier

transfer and reduced the rate of recombination (Fig. 4a) [45]. Similarly, due to the fact that d-CTF also has pyridine N structures, which exhibit lower PL intensity, resulting in reduced electron-hole recombination rates compared to p-CTF and p-CTF-Ni. Mott-Schottky curves provide information about the electrons and the conduction band (CB) [46]. Fig. 4b displays a positive slope, indicating that the catalyst exhibits n-type semiconductor characteristics. As the slope of the curve is directly proportional to the electron concentration (Table S6), the Mott-Schottky equation can be used to estimate the electron concentration in the catalyst [47]. Notably, d-CTF-Ni exhibits the maximum slope, suggesting its highest electron concentration and excellent ability in separating photogenerated electrons and holes. In the UV–visible diffuse reflectance spectra (Fig. S11), all catalysts exhibited absorption characteristics in the visible light region [48]. The presence of Ni atoms and pyridine N enhanced the absorption range, facilitating the generation of additional photogenerated electrons and holes for subsequent redox reactions. Furthermore, the electrochemical impedance spectroscopy (Fig. 4c) and the transient photocurrent response curves (Fig. 4d) showed that d-CTF-Ni exhibited the smallest arc radius and the highest photocurrent density [49], indicating that d-CTF-Ni had the lowest impedance and the fastest electron transfer rate during charge transfer processes. These photoelectric experiments demonstrate the excellent ability of d-CTF-Ni in separating and transferring photogenerated electrons and holes. The presence of Ni atoms and pyridine N structures provides an effective photoelectron basis for the generation of H_2O_2.

3.5. Reaction pathways of Ni single-atom and pyridine N in H_2O_2 production

To investigate the role of the Ni atom and pyridine N in the different pathways of photocatalytic H_2O_2 production, a series of control experiments were carried out. Due to the inhibition of the O_2 reduction pathway upon electron quenching, H_2O_2 generation can only occur through the oxidation pathway of H_2O. To explore the involvement of Ni atoms and pyridine N in the WOR for H_2O_2 production, experiments were conducted to quench the electrons in a continuous flow of Ar gas.
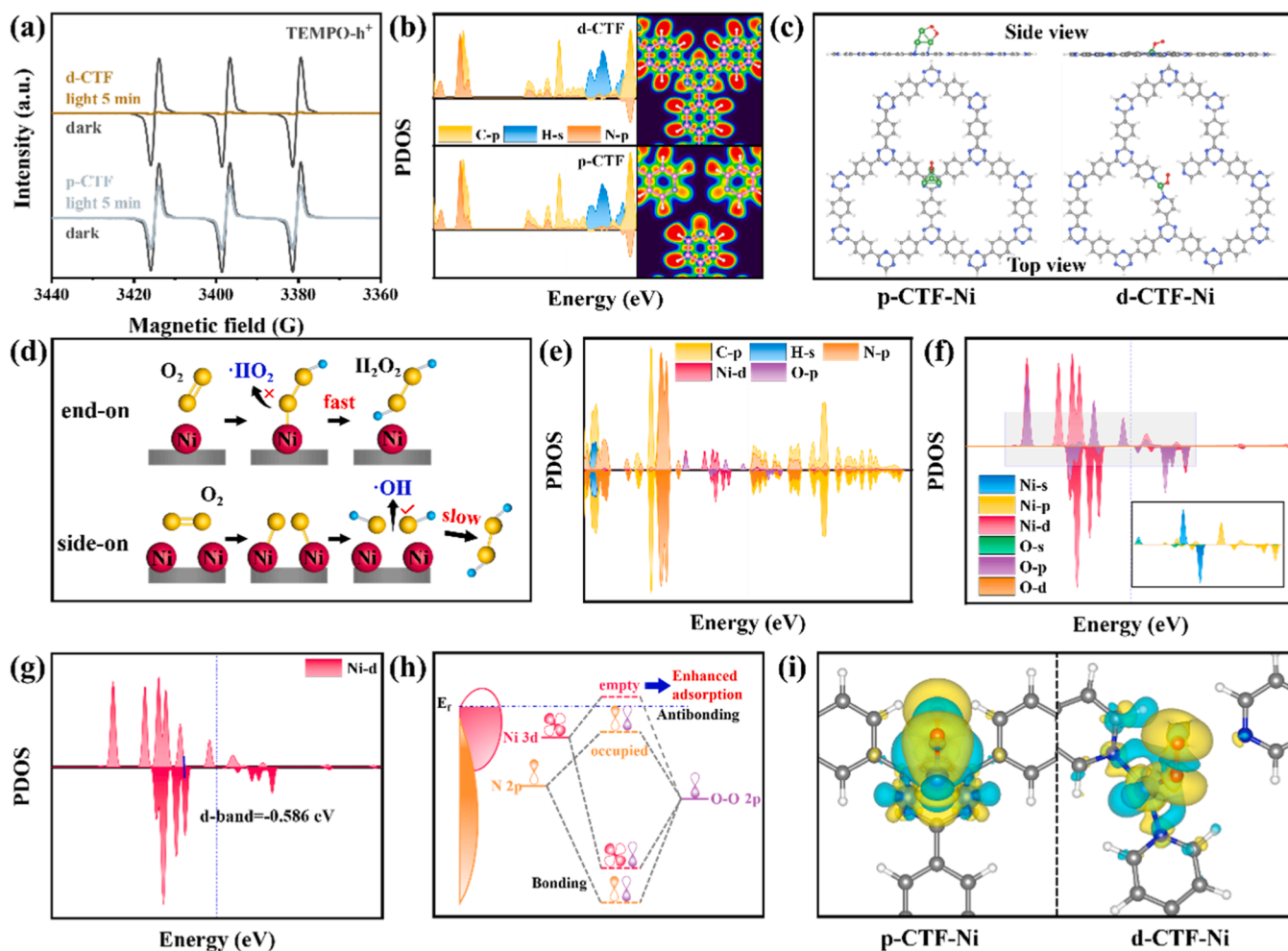
Fig. 6. (a) EPR spectra of the TEMPO-h$^+$. (b) DOS computed with DFT for p-CTF and d-CTF. (c) The adsorption configurations of O_2 on p-CTF-Ni and d-CTF-Ni. (d) Different adsorption behavior of O_2 on Ni atoms and Ni clusters leads to different H_2O_2 production pathways. (e) DOS computed with DFT for d-CTF-Ni after O_2 adsorption. (f) PDOS of the Ni and O orbital. (g) The d-band center of Ni. (h) Schematic of the formation of Ni-O bonds, E_f represents the Fermi level. (i) The electron cloud distribution of p-CTF-Ni and d-CTF-Ni. The yellow represents charge accumulation and the cyan represents charge depletion. The isosurface value is set to 0.001 e·Bohr^{-3}.
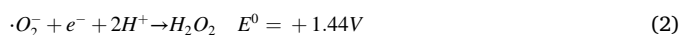
As shown in Fig. 5a, both p-CTF and p-CTF-Ni exhibited a significant decrease in H_2O_2 yield, while d-CTF-Ni showed an approximately 50% decrease, and d-CTF remained almost unchanged. This observation suggests that both p-CTF and p-CTF-Ni exhibit minimal H_2O_2 production through the H_2O oxidation pathway, whereas d-CTF-Ni employs the H_2O oxidation pathway as a significant route for H_2O_2 production. Remarkably, the H_2O oxidation pathway is thoroughly responsible for H_2O_2 generation in d-CTF. Furthermore, under the quenching of holes in an Ar, H_2O_2 production exhibited minimal yields for all catalysts (Fig. S12), providing conclusive evidence that O_2 serves as the primary source for the reduction reaction. Similarly, experiments with continuous O_2 flow to quench the holes were performed to demonstrate the ORR. Fig. 5b illustrates a notable reduction in H_2O_2 production in d-CTF, whereas the H_2O_2 yield in d-CTF-Ni experiences an approximately 50% decrease. Conversely, for p-CTF and p-CTF-Ni, the H_2O_2 level remains nearly constant. This observation suggests that the O_2 reduction pathway predominantly contributes to H_2O_2 generation in p-CTF and p-CTF-Ni and serves as another significant pathway in d-CTF-Ni. Furthermore, the acetonitrile commonly used as a charge transfer insulator, was employed to investigate the role of water [50]. Indeed, as shown in Fig. S13, no H_2O_2 production was observed in the acetonitrile solution after hole quenching, thereby providing compelling evidence that H_2O serves as the source of the oxidation reaction. To sum up, the experiments demonstrated that d-CTF with pyridine N primarily generates

H_2O_2 through the WOR, whereas p-CTF-Ni containing Ni atomic clusters predominantly produces H_2O_2 via the ORR. The d-CTF-Ni exhibited a dual-pathway process, wherein the Ni atoms function as the active reduction centers, while the pyridine N serves as the active oxidation centers.
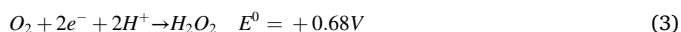
To gain further insights into the specific roles of Ni atoms and pyridine N in their respective pathways, a detailed investigation of the reaction process was conducted. The energy band structures of the catalysts were determined through photoelectric experiments, as shown in Fig. S14. The CB values of p-CTF and p-CTF-Ni exhibit greater negativity, being smaller than − 0.33 V, which suggests the coexistence of both direct and indirect 2e$^-$-ORR pathways in them. In contrast, the CB value of d-CTF and d-CTF-Ni lies within the range of − 0.33 V to 0.68 V, indicating that only the direct 2e$^-$-ORR pathway is thermodynamically favorable in these cases [51]. In general, Eqs. (1)–(2) are associated with the indirect 2e$^-$-ORR, while Eq. (3) corresponds to the direct 2e$^-$-ORR, wherein the presence of the intermediate product·O_2^- serves as a distinguishing factor between these direct and indirect reactions. To verify the specific case of ORR, EPR tests were conducted on p-CTF, p-CTF-Ni, and d-CTF-Ni, which predominantly underwent ORR reactions to detect intermediates·HO$_2$/·O_2^- (·HO$_2$,·O_2^-+H$^+$→·HO$_2$) [52]. Fig. 5c shows that p-CTF and p-CTF-Ni both exhibit DMPO-·HO$_2$/·O_2^- signals compared to d-CTF-Ni, providing evidence for the presence of intermediate species·O_2^- in irradiated p-CTF and p-CTF-Ni. Furthermore,

the intensity of DMPO-·HO$_2$/·O$_2^-$ is significantly lower in p-CTF-Ni compared to p-CTF, which suggests that the presence of Ni reduces the occurrence of intermediate species·O$_2^-$, favoring the direct 2e$^-$-ORR process, while the p-CTF without active centers still tends to undergo ORR. Subsequently, quenching experiments were conducted to further verify whether the intermediate species·O$_2^-$ was involved in H$_2$O$_2$ production. Fig. 5d demonstrates a significant reduction in the yield of H$_2$O$_2$ in p-CTF and p-CTF-Ni after·O$_2^-$ quenching, while the variation in d-CTF-Ni can be neglected. The results of EPR and quenching experiments indicate that the H$_2$O$_2$ production process of p-CTF and p-CTF-Ni undergo indirect 2e$^-$-ORR judged from the existence of·O$_2^-$, resulting in a slower rate of H$_2$O$_2$ generation. Moreover, the presence of Ni in p-CTF-Ni and d-CTF-Ni allows for more favorable low-energy barriers (-0.68 V for direct 2e$^-$-ORR vs -1.44 V for indirect 2e$^-$-ORR) and facilitates the accelerated production of H$_2$O$_2$ through direct 2e$^-$-ORR.

Indirect ORR:

$$O_2 + e^- \rightarrow \cdot O_2^- \quad E^0 = -0.33V \tag{1}$$

$$\cdot O_2^- + e^- + 2H^+ \rightarrow H_2O_2 \quad E^0 = +1.44V \tag{2}$$

Direct ORR:

$$O_2 + 2e^- + 2H^+ \rightarrow H_2O_2 \quad E^0 = +0.68V \tag{3}$$
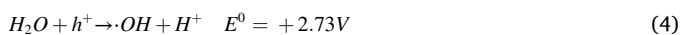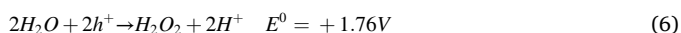
Furthermore, the valence band (VB) values of the catalysts are all higher than 1.76 V, suggesting their inherent capability for the indirect H$_2$O oxidation (H$_2$O→·OH) pathway, wherein the produced·OH species can subsequently couple with another·OH to yield H$_2$O$_2$. To demonstrate the specific pathway of the WOR, EPR tests (Fig. 5e) and quenching experiments (Fig. 5f) similar to·O$_2^-$ were conducted on d-CTF and d-CTF-Ni which predominantly carries out WOR. The EPR test results provide direct evidence for the absence of intermediate species·OH in the WOR process. In fact, due to the presence of hole acceptors in d-CTF and d-CTF-Ni, the H$_2$O oxidation pathway mainly proceeds through the direct reaction shown in Eq. (6), which encounters a low energy barrier that facilitates the rapid production of H$_2$O$_2$. As a whole, the structures of pyridine N in the catalyst promotes the occurrence of low-energy barrier reactions (1.76 V for direct 2e$^-$-WOR vs 2.73 V for indirect 2e$^-$-WOR), thereby increasing the production of H$_2$O$_2$.

Indirect WOR:

$$H_2O + h^+ \rightarrow \cdot OH + H^+ \quad E^0 = +2.73V \tag{4}$$

$$\cdot OH + \cdot OH \rightarrow H_2O_2 \tag{5}$$

Direct WOR:

$$2H_2O + 2h^+ \rightarrow H_2O_2 + 2H^+ \quad E^0 = +1.76V \tag{6}$$

Due to the extremely short lifetimes of active species, they tend to preferentially participate in kinetically favored reactions, thereby excluding intrinsic reactions involving free radicals. Therefore, experimental evidence has demonstrated that Ni atoms serve as active reduction centers for direct 2e$^-$-ORR, while pyridine N acts as active oxidation centers for direct 2e$^-$-WOR. For d-CTF-Ni, the dual active sites comprising Ni atoms and pyridine N facilitate low-energy barrier reactions in a dual-pathway, thereby accelerating the production of H$_2$O$_2$.

3.6. Critical role of Ni single-atom and pyridine N in the production of H$_2$O$_2$

Building upon the demonstrated roles of pyridine N and Ni atoms in promoting direct reactions of H$_2$O$_2$ production during the H$_2$O oxidation and O$_2$ reduction pathways, respectively, comprehensive insights into the intrinsic mechanism for the enhancement of redox processes by pyridine N and Ni atoms are explored through DFT calculations.

From one side, the involvement of pyridine N in facilitating the direct 2e$^-$-WOR process is unveiled. Based on structural analysis, it was

confirmed that d-CTF is almost identical to p-CTF in composition and structure, except for the introduction of pyridine N. To further understand the role of pyridine N in the photocatalytic production of H$_2$O$_2$, electron spin resonance (ESR) tests were conducted (Fig. 6a). Compared to p-CTF, the signal of d-CTF exhibited significant decay after irradiation, indicating enhanced binding of the paramagnetic scavenger TEMPO with more photogenerated holes, leading to a reduction in the signal [53]. These results suggest that the pyridine N structure in d-CTF possesses stronger hole-trapping capability. And the density of states (DOS) plot also confirms the weakening of electrons near the pyridine N (Fig. 6b). The transfer of photogenerated electrons was analyzed through DFT calculations of Bader charges. The results reveal the charge in the N reduced from 8.134 in p-CTF to 6.948 in d-CTF (Table S7), providing evidence of electron depletion [54], which suggests that the presence of the pyridine N in d-CTF facilitates the trapping of holes. Therefore, pyridine N serves as a center for active oxidation by capturing more photogenerated holes and enhancing the photocatalytic reaction through the low-energy barriers, thereby facilitating the photocatalytic generation of H$_2$O$_2$.

On the other side, the mechanism by which Ni atoms promote direct 2e$^-$-ORR is particularly investigated. Considering that the adsorption of O$_2$ on Ni atoms is the first step in the participation of O$_2$ in ORR, to investigate the mechanism by which the presence of Ni atoms leads to the enhancement of photocatalytic H$_2$O$_2$ generation, the adsorption behavior of O$_2$ on the Ni-based catalyst was examined using DFT. Fig. 6c shows the distinct adsorption configuration of O$_2$ on p-CTF-Ni and d-CTF-Ni, characterized by a higher propensity for "side-on" adsorption on p-CTF-Ni and a greater inclination for "end-on" adsorption on d-CTF-Ni. In general, the ability of catalyst to dissociate the O=O bond is often considered the rate-limiting step in the ORR process, and the breaking of the O-O bond further hinders the generation of H$_2$O$_2$ [55]. Bader charge analysis reveals that upon adsorption of O$_2$ in "side-on" and "end-on" configurations on p-CTF-Ni and d-CTF-Ni, the electrons on O$_2$ increase by 0.484 |e| and 0.781 |e|, respectively, while the adsorption energies of O$_2$ on the surfaces are 1.14 eV and 2.40 eV, respectively. This indicates that O$_2$ can be readily activated on Ni-based catalysts, signifying the facile cleavage of the O=O bond. Furthermore, the O=O bond length (originally 1.20 Å) extends to 1.886 Å and 1.783 Å following adsorption of O$_2$ on p-CTF-Ni and d-CTF-Ni, which suggest that the "end-on" adsorption configuration leads to a stronger interaction between the O atoms, whereas the "side-on" adsorption configuration on the Ni clusters exhibits a relatively weaker binding, thus favoring O-O bond cleavage [56]. Therefore, the adsorption of O$_2$ on Ni-based catalysts facilitates its activation, resulting in the cleavage of the O=O bond, while the weaker "side-on" adsorption configuration on Ni clusters leads to the formation of other intermediate species after the conversion of O=O to O-O. In this process, the intermediate species·OH is likely to occur before the formation of H$_2$O$_2$. As shown in Fig. S15, a distinct DMPO-·OH signal was observed in p-CTF-Ni, confirming the presence of the intermediate species·OH in the photocatalytic production of H$_2$O$_2$ and supporting the "side-on" adsorption of O$_2$. Different forms of Ni atoms on the catalyst surface have varying influences on the adsorption configuration, thereby altering the reaction pathway for the photocatalytic generation of H$_2$O$_2$. Consequently, the Ni atom in d-CTF-Ni exhibits an "end-on" adsorption configuration for O$_2$, which mitigates the break of the O-O bond and hinders the formation of intermediate species·HO$_2$/·O$_2^-$ and·OH, thus accelerating the production of H$_2$O$_2$ through one-step direct 2e$^-$-ORR (Fig. 6d). To gain insight into the mechanism by which Ni single atoms lead to enhanced photocatalytic H$_2$O$_2$ production, the electron transfer within Ni-based catalysts was investigated using DFT. Bader charge analysis demonstrates that Ni single atoms exhibit a greater degree of electron transfer upon O$_2$ adsorption. Moreover, the density of states (DOS) plot reveals the emergence of a new energy band upon the introduction of Ni atoms (Fig. 6e), indicating that the presence of Ni atoms provides a step for electron transfer. Considering that the catalytic performance is governed by the electronic structure, thus the
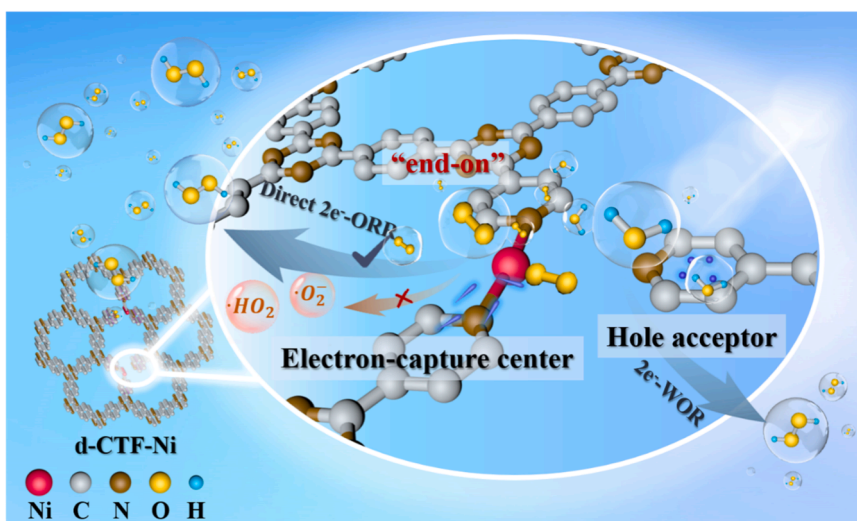
Fig. 7. Schematic illustration of d-CTF-Ni for photocatalytic H_2O_2 production.

presence of Ni atoms is crucial for efficient photocatalytic production of H_2O_2. To investigate the interaction between Ni and O atoms, the comparison of the partial density of states (PDOS) between Ni and O was performed, as shown in Fig. 6f. The energy levels of the Ni-d band align closely with the O-p band, indicating a significant p-d orbital hybridization between Ni and O atoms [57]. This hybridization results in the redistribution of electrons within Ni, providing further evidence for charge transfer between Ni and O. It is worth noting that the calculated center of the Ni d-band is close to the Fermi level (Fig. 6g), which indicates in the presence of adsorbed $*O_2$, the occupancy of the antibonding orbitals of Ni decreases, thereby promoting the adsorption of $*O_2$. When O_2 is adsorbed on the Ni atoms, electrons transfer from the d-p π antibonding orbitals of the Ni-O bond to partially occupied d-bands [58], as shown in Fig. 6h. Furthermore, the electron cloud distributions of the theoretical models p-CTF-Ni and d-CTF-Ni after O_2 adsorption were investigated (Fig. 6i, Fig. S16-**17**), there is a significant accumulation of electrons around the adsorbed $*O_2$, with a corresponding depletion of electrons around the Ni and pyridine N atoms [59,60]. Importantly, the electron cloud between $*O_2$ and the Ni surface is more pronounced in the Ni atoms than in the Ni atom clusters, indicating that electrons readily transfer from partially occupied d orbitals of Ni atoms to the vacant 2p orbitals of the O_2 molecule. Theoretical calculations confirm that the isolated Ni atom provides a directional pathway (Ni→O_2) for electron transfer, and that Ni atoms act as electron-capture centers to transfer a large number of electrons to adsorbed $*O_2$, thereby facilitating the reduction of O_2 and the rapid generation of H_2O_2.

Based on the analysis above, the following reaction mechanism is proposed as shown in Fig. 7. Firstly, d-CTF-Ni generates a substantial number of electrons and holes under visible light irradiation. Subsequently, the photogenerated holes primarily localized at the pyridine nitrogen sites facilitate the oxidation of H_2O molecules at low energy barriers, thereby promoting the generation of H_2O_2. Simultaneously, O_2 molecules adsorb in an "end-on" configuration onto Ni atom sites and undergo reduction through the directed migration of photogenerated electrons, resulting in the continuous production of H_2O_2. It is noteworthy that the separated photogenerated electron and hole centers effectively participate in their respective reduction and oxidation reactions, and this synergistic dual-pathway enhances the production of H_2O_2.

4. Conclusion

In summary, the introduction of atomically dispersed Ni at the CTF defect site and the exposure of pyridine N at the defect edge results in

significant changes in the active centers and the original electronic structure. The d-CTF-Ni allows Ni single atoms as electron-capture centers to form a directional pathway (Ni→O_2) for the reduction of O_2 through electron transfer, completing the O_2 reduction reaction (O_2 +2e$^-$+2 H$^+$→H_2O_2). And enabling the pyridine N sites to serve as hole acceptors to increases the hole content thereby enhance the oxidation reaction of H_2O (2 H_2O+2 h$^+$→H_2O_2 +2 H$^+$), where the synergistic direct reaction promotes the dual-pathway production of H_2O_2. Moreover, the independent redox centers further enhance the separation of photogenerated electrons and holes, exhibiting significant potential for efficient H_2O_2 production. Additionally, H_2O_2 stands as one of the most commonly employed disinfectants, but its large-scale production continues to rely on the anthraquinone process, which involves the use and generation of hazardous substances. This study not only avoids the need for sacrificial agents through the utilization of clean energy sources, but also offers valuable insights into exploring potential dual-pathway mechanisms for enhanced H_2O_2 generation. The findings of this research aim to offer inspiration for the clean industrial-scale production of H_2O_2 through photocatalysis.

CRediT authorship contribution statement

Shasha Liu: Writing - original draft, Conceptualization, Data curation, Software. **Chao Zhu:** Methodology, Computational modeling, Writing & editing. **Jujie Xu:** Data curation, Software. **Lun Lu:** Computational modeling. **Qile Fang:** Computational modeling. **Chao Xu:** Supervision. **Yong Zheng:** Software. **Shuang Song:** Review & editing. **Yi Shen:** Supervision, Funding acquisition, Resources, Writing-review & editing.

Declaration of Competing Interest

The authors declare that they have no known competing financial interests or personal relationships that could have appeared to influence the work reported in this paper.

Data Availability

I have share the link to my data/code at the Attach File step.

Acknowledgements

Appendix A. Supporting information

Supplementary data associated with this article can be found in the online version at doi:10.1016/j.apcatb.2023.123629.

References

[1] Y. Shen, Y. Yao, C. Zhu, J. Wu, L. Chen, Q. Fang, S. Song, Unveiling excitonic effect-regulated singlet oxygen generation towards efficient photocatalytic H_2O_2 production, Chem. Eng. J. 475 (2023), 146383..

[2] T. Liu, Z. Pan, J.J.M. Vequizo, K. Kato, B. Wu, A. Yamakata, K. Katayama, B. Chen, C. Chu, K. Domen, Overall photosynthesis of H_2O_2 by an inorganic semiconductor, Nat. Commun. 13 (2022) 1034.

[3] L. Wang, J. Zhang, Y. Zhang, H. Yu, Y. Qu, J. Yu, Inorganic metal-oxide photocatalyst for H_2O_2 production, Small 18 (2022), 2104561.

[4] H. Hou, X. Zeng, X. Zhang, Production of hydrogen peroxide by photocatalytic processes, Angew. Chem. Int. Ed. 59 (2020) 17356–17376.

[5] F.-Y. Yu, Y.-J. Zhou, H.-Q. Tan, Y.-G. Li, Z.-H. Kang, Versatile photoelectrocatalysis strategy raising up the green production of hydrogen peroxide, Adv. Energy Mater. 13 (2023), 2300119.

[6] J. Chang, Q. Li, J. Shi, M. Zhang, L. Zhang, S. Li, Y. Chen, S. Li, Y. Lan, Oxidation-reduction molecular junction covalent organic frameworks for full reaction photosynthesis of H_2O_2, Angew. Chem. Int. Ed. 62 (2023), e2022188.

[7] S. Chen, T. Luo, X. Li, K. Chen, J. Fu, K. Liu, C. Cai, Q. Wang, H. Li, Y. Chen, C. Ma, L. Zhu, Y.-R. Lu, T.-S. Chan, M. Zhu, E. Cortés, M. Liu, Identification of the highly active Co–N_4 coordination motif for selective oxygen reduction to hydrogen peroxide, J. Am. Chem. Soc. 144 (2022) 14505–14516.

[8] Y. Wu, J. Chen, H. Che, X. Gao, Y. Ao, P. Wang, Boosting 2e⁻ oxygen reduction reaction in garland carbon nitride with carbon defects for high-efficient photocatalysis-self-Fenton degradation of 2, 4-dichlorophenol, Appl. Catal. B: Environ. 307 (2022), 121185.

[9] J. Luo, C. Fan, L. Tang, Y. Liu, Z. Gong, T. Wu, X. Zhen, C. Feng, H. Feng, L. Wang, L. Xu, M. Yan, Reveal Brønsted–Evans–Polanyi relation and attack mechanisms of reactive oxygen species for photocatalytic H_2O_2 production, Appl. Catal. B: Environ. 301 (2022), 120757.

[10] M. Song, W. Liu, J. Zhang, C. Zhang, X. Huang, D. Wang, Single-atom catalysts for H_2O_2 electrosynthesis via two-electron oxygen reduction reaction, Adv. Funct. Mater. 33 (2023), 2212087.

[11] J. Xiao, Q. Liu, M. Song, X. Li, Q. Li, J.K. Shang, Directing photocatalytic pathway to exceedingly high antibacterial activity in water by functionalizing holey ultrathin nanosheets of graphitic carbon nitride, Water Res 198 (2021), 117125.

[12] L. Liu, M.-Y. Gao, H. Yang, X. Wang, X. Li, A.I. Cooper, Linear conjugated polymers for solar-driven hydrogen peroxide production: the importance of catalyst stability, J. Am. Chem. Soc. 143 (2021) 19287–19293.

[13] Y. Xue, Y. Wang, Z. Pan, K. Sayama, Electrochemical and photoelectrochemical water oxidation for hydrogen peroxide production, Angew. Chem. Int. Ed. 60 (2021) 10469–10480.

[14] C. Wu, Z. Teng, C. Yang, F. Chen, H.B. Yang, L. Wang, H. Xu, B. Liu, G. Zheng, Q. Han, Polarization engineering of covalent triazine frameworks for highly efficient photosynthesis of hydrogen peroxide from molecular oxygen and water, Adv. Mater. 34 (2022), 2110266.

[15] Z. Chen, D. Yao, C. Chu, S. Mao, Photocatalytic H_2O_2 production systems: design strategies and environmental applications, Chem. Eng. J. 451 (2023), 138489.

[16] L. Fang, T. Huang, H. Lu, X. Wu, Z. Chen, H. Yang, S. Wang, Z. Tang, Z. Li, B. Hu, X. Wang, Biochar-based materials in environmental pollutant elimination, H2 production and CO2 capture applications, Biochar 5 (2023) 42.

[17] T. He, J. Wu, Y. Li, K. Wei, Y. Liu, H. Huang, Y. Liu, Z. Kang, A step-by-step design for dual channel metal-free photocatalysts towards high yield H_2O_2 photo-production from air and water, Chem. Eng. J. 451 (2023), 138551.

[18] Y. Li, Y. Zhao, J. Wu, Y. Han, H. Huang, Y. Liu, Z. Kang, Photo-charge regulation of metal-free photocatalyst by carbon dots for efficient and stable hydrogen peroxide production, J. Mater. Chem. A 9 (2021) 25453–25462.

[19] Z. Chen, Y. Li, Y. Cai, S. Wang, B. Hu, B. Li, X. Ding, Li Zhuang, X. Wang, Application of covalent organic frameworks and metal–organic frameworks nanomaterials in organic/inorganic pollutants removal from solutions through sorption-catalysis strategies, Carbon Res. 8 (2023) 2.

[20] Y. Shen, J. Hu, L. Lu, C. Zhu, Q. Fang, S. Song, Enhanced photocatalytic performance of S-doped covalent triazine framework for organic pollutant degradation, J. Zhejiang Univers. Sci. A 23 (2022) 988–997.

[21] X. Hu, Z. Zhan, J. Zhang, I. Hussain, Immobilized covalent triazine frameworks films as effective photocatalysts for hydrogen evolution reaction, Nat. Commun. 12 (2021) 6596.

[22] C. Zhu, L. Lu, Q. Fang, S. Song, B. Chen, Y. Shen, Unveiling spin state-dependent Micropollutant removal using single-atom covalent triazine framework, Adv. Funct. Mater. 33 (2023), 2210905.

[23] Z. Gu, J. Wang, Z. Shan, M. Wu, T. Liu, L. Song, G. Wang, X. Ju, J. Su, G. Zhang, Modulating electronic structure of triazine-based covalent organic frameworks for photocatalytic organic transformations, J. Mater. Chem. A 10 (2022) 17624–17632.

[24] X. Lan, X. Liu, Y. Zhang, Q. Li, J. Wang, Q. Zhang, G. Bai, Unveiling charge dynamics in acetylene-Bridged donor–π–acceptor covalent triazine framework for enhanced photoredox catalysis, ACS Catal. 11 (2021) 7429–7441.

[25] Y. Shen, S. Liu, L. Lu, C. Zhu, Q. Fang, R. Liu, Y. Shen, S. Song, Pyridine-linked covalent triazine frameworks with bidirectional electron donor-acceptor for efficient organic pollution removal, J. Hazard. Mater. 444 (2023), 130428.

[26] Y. Li, C. Lai, S. Liu, Y. Fu, L. Qin, M. Xu, D. Ma, X. Zhou, F. Xu, H. Liu, L. Li, S. Qian, N. Wang, Metallic active-site engineering: a bridge between covalent triazine frameworks and high-performance catalysts, J. Mater. Chem. A 11 (2023) 2070.

[27] C. Yang, X. Hu, Y. Bai, B. Cai, Y. Li, Fe single atoms reduced by NaBH₄ mediate g-C₃N₄ electron transfer and effectively remove 2-mercaptobenzothiazole, Catalysts 13 (2023) 619.

[28] Y. Zhao, Y. Liu, J. Cao, H. Wang, M. Shao, H. Huang, Y. Liu, Z. Kang, Efficient production of H_2O_2 via two-channel pathway over ZIF-8/C₃N₄ composite photocatalyst without any sacrificial agent, Appl. Catal. B: Environ. 287 (2020), 119289.

[29] R. Ma, L. Wang, H. Wang, Z. Liu, M. Xing, L. Zhu, X. Meng, F.-S. Xiao, Solid acids accelerate the photocatalytic hydrogen peroxide synthesis over a hybrid catalyst of titania nanotube with carbon dot, Appl. Catal. B: Environ. 244 (2019) 594–603.

[30] J. Cao, H. Wang, Y. Zhao, Y. Liu, Q. Wu, H. Huang, M. Shao, Yang Liu, Z. Kang, Phosphorus-doped porous carbon nitride for efficient sole production of hydrogen peroxide via photocatalytic water splitting with a two-channel pathway, J. Mater. Chem. A 8 (2020) 3701–3707.

[31] C. Zhu, L. Lu, J. Xu, S. Song, Q. Fang, R. Liu, Y. Shen, J. Zhao, W. Dong, Y. Shen, Metal monovacancy-induced spin polarization for simultaneous energy recovery and wastewater purification, Chem. Eng. J. 451 (2023), 138537.

[32] Y. Chang, H. Huang, H. Zhu, Y. Zhao, L. Wang, Y. Sun, C. Zhong, Robust carbazole-based covalent triazine frameworks with defective ultramicropore structure for efficient ethane-selective ethane-ethylene separation, Chem. Eng. J. 427 (2022), 131726.

[33] Y. Shen, H. Zhang, B. Chen, C. Zhu, W. Yu, J. Yang, Q. Fang, Z. He, T. Sun, S. Song, Mechanistic insight into electron orientation by tailoring Ni–Cu atom-pairs for high-performance CO₂ electroreduction, Appl. Catal. B: Environ. 330 (2023), 122654.

[34] M. Liu, Q. Huang, S. Wang, Z. Li, B. Li, S. Jin, B. Tan, Crystalline covalent triazine frameworks by in situ oxidation of alcohols to aldehyde monomers, Angew. Chem. Int. Ed. 57 (2018) 11968–11972.

[35] S. Zhang, G. Cheng, L. Guo, N. Wang, B. Tan, S. Jin, Strong-base-assisted synthesis of a crystalline covalent triazine framework with high hydrophilicity via benzylamine monomer for photocatalytic water splitting, Angew. Chem. Int. Ed. 59 (2020) 6007–6014.

[36] Y. Shen, C. Zhu, S. Song, T. Zeng, L. Li, Z. Cai, Defect-abundant covalent triazine frameworks as sunlight-driven self-cleaning adsorbents for volatile aromatic pollutants in water, Environ. Sci. Technol. 53 (2019) 9091–9101.

[37] C. Zhu, Q. Fang, R. Liu, W. Dong, S. Song, Y. Shen, Insights into the crucial role of electron and spin structures in heteroatom-doped covalent triazine frameworks for removing organic micropollutants, Environ. Sci. Technol. 56 (2022) 6699–6709.

[38] Y. Zheng, H. Song, S. Chen, X. Yu, J. Zhu, J. Xu, K.A.I. Zhang, Z. Tang, T. Liu, Metal-free multi-heteroatom-doped carbon bifunctional electrocatalysts derived from a covalent triazine polymer, Small 16 (2020), 2004342–2004352.

[39] J. Xu, Y. Yao, C. Zhu, L. Lu, Q. Fang, Z. He, S. Song, B. Chen, Y. Shen, Unveiling enhanced electron-mediated peroxymonosulfate activation for degradation of emerging organic pollutants, Appl. Catal. B Environ. 341 (2024), 123356.

[40] Y. Shen, J. Yang, C. Zhu, Q. Fang, S. Song, B. Chen, Mechanistic insights into the atomic distance effect on adsorption and degradation of aromatic compounds, ACS Catal. 13 (2023) 8943–8954.

[41] W. Zhong, R. Sa, L. Li, Y.0 He, L. Li, J. Bi, Z. Zhuang, Y. Yu, Z. Zou, A covalent organic framework bearing single Ni sites as a synergistic photocatalyst for selective photoreduction of CO₂ to CO, J. Am. Chem. Soc. 141 (2019) 7615–7621.

[42] Y. Shen, S. Liu, L. Lu, C. Zhu, Q. Fang, R. Liu, Z. He, Y. Li, S. Song, Photocatalytic degradation of toluene by a TiO₂ p-n homojunction nanostructure, ACS Appl. Nano Mater. 5 (2022) 18612–18621.

[43] Y. Shen, Y. Yao, L. Lu, C. Zhu, Q. Fang, J. Wang, S. Song, Insights into dual effect of missing linker-cluster domain defects for photocatalytic 2e⁻ ORR: Radical reaction and electron behavior, Chemosphere 324 (2023), 138220.

[44] R. Liu, J. Ma, X. Zheng, M. Zhao, C. Zhu, Y. Shen, Enhanced electrochemical degradation of aromatic organic pollutants through accelerated electron transfer using Fe-C structured rGO/Fe-NF, Sep. Purif. Technol. 330 (2024), 125269.

[45] Z. Wei, W. Wang, W. Li, X. Bai, J. Zhao, E.C.M. Tse, D.L. Phillips, Y. Zhu, Steering electron–hole migration pathways using oxygen vacancies in tungsten oxides to enhance their photocatalytic oxygen evolution performance, Angew. Chem. Int. Ed. 60 (2021) 8236–8242.

[46] S. Liu, L. Lu, C. Zhu, Q. Fang, S. Song, Y. Zheng, Y. Shen, The role of dual vacancies in TiO₂ for enhanced photocatalytic hydrogen generation and pollutants removal, ChemCatChem 14 (2022), e202201107.

[47] Z. Kong, L. Lu, C. Zhu, J. Xu, Q. Fang, R. Liu, Y. Shen, Enhanced adsorption and photocatalytic removal of PFOA from water by F-functionalized MOF with in-situ-growth TiO₂: regulation of electron density and bandgap, Sep. Purif. Technol. 297 (2022) 121449.

[48] J. Xu, C. Zhu, S. Song, Q. Fang, J. Zhao, Y. Shen, A nanocubicle-like 3D adsorbent fabricated by in situ growth of 2D heterostructures for removal of aromatic contaminants in water, J. Hazard. Mater. 423 (2022) 127004.

[49] K. Chen, G. Zhang, L. Xiao, P. Li, W. Li, Q. Xu, J. Xu, Polyaniline encapsulated amorphous V_2O_5 nanowire-modified multi-functional separators for lithium-sulfur batteries, Small 5 (2021), 2001056.

[50] S. Chugh, N. Adhikari, J.H. Lee, D. Berman, L. Echegoyen, A.B. Kaul, Dramatic enhancement of optoelectronic properties of electrophoretically deposited C_{60}–graphene hybrids, ACS Appl. Mater. Interfaces 11 (2019) 24349–24359.

[51] Y. Luo, B. Zhang, C. Liu, D. Xia, X. Ou, Y. Cai, Y. Zhou, J. Jiang, B. Han, Sulfone-modified covalent organic frameworks enabling efficient photocatalytic hydrogen peroxide generation via one-step two-electron O_2 reduction, Angew. Chem. Int. Ed. 62 (2023), e2023053.

[52] M. Xu, Y. Zhang, H. Yin, J. Wang, A. Li, P.F.-X. Corvini, Efficient catalytic ozonation over Co-ZFO@ Mn-CN for oxalic acid degradation: Synergistic effect of oxygen vacancies and HOO-Mn-N-X bonds, Appl. Catal. B: Environ. 322 (2023), 122085.

[53] L. Luo, Z. Gong, Y. Xu, J. Ma, H. Liu, J. Xing, J. Tang, Binary Au–Cu reaction sites decorated ZnO for selective methane oxidation to C1 oxygenates with nearly 100% selectivity at room temperature, J. Am. Chem. Soc. 144 (2022) 740–750.

[54] J. Xu, C. Zhu, R. Liu, Q. Fang, Y. Zheng, Z. He, S. Song, Yi Shen, Elucidating the charge redistribution in bimetallic metal-organic frameworks: High-electron-density reactive center for removal of organic micropollutants in water, Chem. Eng. J. 468 (2023), 143723.

[55] C.H. Choi, H.C. Kwon, S. Yook, H. Shin, H. Kim, M. Choi, Hydrogen peroxide synthesis via enhanced two-electron oxygen reduction pathway on carbon-coated Pt surface, J. Phys. Chem. C. 118 (2014) 30063–30070.

[56] Y. Yao, J. Yang, C. Zhu, L. Lu, Q. Fang, C. Xu, Z. He, S. Song, Y. Shen, Unveiling the metallic size effect on O_2 adsorption and activation for enhanced electro-Fenton degradation of aromatic compounds, J. Hazard. Mater. 462 (2024), 132739.

[57] H. Ou, S. Ning, P. Zhu, S. Chen, A. Han, Q. Kang, Z. Hu, J. Ye, D. Wang, Y. Li, Carbon nitride photocatalysts with integrated oxidation and reduction atomic active centers for improved CO_2 conversion, Angew. Chem. Int. Ed. 61 (2022), e202206579.

[58] J. Xu, L. Lu, C. Zhu, Q. Fang, R. Liu, D. Wang, Z. He, S. Song, Y. Shen, Insights into conduction band flexibility induced by spin polarization in titanium-based metal-organic frameworks for photocatalytic water splitting and pollutants degradation, J. Colloid. Interf. Sci. 630 (2023) 430–442.

[59] X. Yang, R. Wang, S. Wang, C. Song, S. Lu, L. Fang, F. Yin, H. Liu, Sequential active-site switches in integrated Cu/Fe-TiO$_2$ for efficient electroreduction from nitrate into ammonia, Appl. Catal. B: Environ. 325 (2023), 122360.

[60] Y. Shen, J. Wu, C. Zhu, J. Zhao, Q. Fang, Y. Zheng, C.T.J. Ferguson, S. Song, Bifunctional covalent triazine frameworks based on Ti-ON bonds for micropollutants removal: effects of 3D extended structure and electron transport bridges, Chem. Eng. J. 465 (2023), 143026.